J. Am. Soc. Mass Spectrom. (2018) 29:1791–1801
DOI: 10.1007/s13361-018-1959-1

FOCUS: APPLICATION OF PHOTONS AND RADICALS FOR MS: RESEARCH ARTICLE

Radical Rearrangement Chemistry in Ultraviolet Photodissociation of Iodotyrosine Systems: Insights from Metastable Dissociation, Infrared Ion Spectroscopy, and Reaction Pathway Calculations

Karnamohit Ranka,[1,2] Ning Zhao,[3] Long Yu,[3] John F. Stanton,[1,2] Nicolas C. Polfer[3]

[1]Quantum Theory Project, Department of Chemistry, University of Florida, P.O. Box 117200, Gainesville, FL 32611-7200, USA
[2]Quantum Theory Project, Department of Physics, University of Florida, P.O. Box 118435, Gainesville, FL 32611-8435, USA
[3]Department of Chemistry and Center for Chemical Physics, University of Florida, P.O. Box 117200, Gainesville, FL 32611-7200, USA

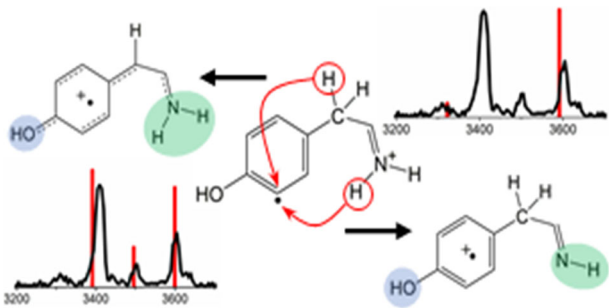

Abstract. We report on the ultraviolet photodissociation (UVPD) chemistry of protonated tyrosine, *iodo*tyrosine, and *diiodo*tyrosine. Distonic loss of the iodine creates a high-energy radical at the aromatic ring that engages in hydrogen/proton rearrangement chemistry. Based on UVPD kinetics measurements, the appearance of this radical is coincident with the UV irradiation pulse (8 ns). Conversely, sequential UVPD product ions exhibit metastable decay on ca. 100 ns timescales. Infrared ion spectroscopy is capable of confirming putative structures of the rearrangement products as proton transfers from the imine and β-carbon hydrogens. Potential energy surfaces for the various reaction pathways indicate that the rearrangement chemistry is highly complex, compatible with a cascade of rearrangements, and that there is no preferred rearrangement pathway even in small molecular systems like these.

Keywords: UVPD, Kinetics, IRMPD spectroscopy, DFT, Metastable decay

Received: 26 February 2018/Revised: 21 March 2018/Accepted: 1 April 2018/Published Online: 29 May 2018

Introduction

It is well documented that radical dissociation chemistry can be useful in sequencing mass spectrometry, as the fragmentation process gives rise to efficient backbone cleavages, while at the same time conserving information on labile groups, such as post-translational modifications (PTMs) in peptides and proteins [1]. The growth in electron capture dissociation (ECD) [2, 3] and later electron transfer dissociation (ETD) [4, 5] is linked to their contributions for enhanced sequencing capabilities in mass spectrometry, especially in proteomics.

More recently, ultraviolet photodissociation (UVPD) has gained attention as an ion activation technique [6–11], even if its first implementation dates three decades ago [12, 13]. In UVPD, an ion is electronically excited with photons from an intense light source, usually a laser. The dissociation chemistry that takes place is often different and generally more selective than simply "heating" up the ions by collisions or infrared photons. For instance, preferred bond cleavages at disulfide bonds [11] and preferential backbone cleavages, as opposed to the loss of fragile side-chain groups [6], are all testament to the different dissociation pathways that can be accessed via electronic excitation. While the exact mechanism remains a matter of debate [14], the fragmentation chemistry in UVPD has

Karnamohit Ranka and Ning Zhao contributed equally.

Electronic supplementary material The online version of this article (https://doi.org/10.1007/s13361-018-1959-1) contains supplementary material, which is available to authorized users.

Correspondence to: Nicolas Polfer; *e-mail:* polfer@chem.ufl.edu

similarities with processes observed in the radical-driven ECD and ETD [15, 16].

UVPD in principle presents some more unique characteristics that may aid a mechanistic understanding. Ion activation takes place at a well-defined time (on a nanosecond timescale) and therefore lends itself to kinetic studies. Moreover, the incorporation of photolabile groups, such as C–I bonds, can give rise to photolysis and generation of a radical species at a known site [17]. It should be noted that in some molecular systems, radical ions can be generated by collisional activation as well [18–22]. Nonetheless, UV activation is generally more specific, since from a photophysics perspective, the absorption of a UV photon initially accesses a bound singlet ππ* state, followed by curve crossing to a dissociative triplet πσ* state localized on the C–I bond [23]. As pioneered by Ryan Julian, winner of the *2017 Biemann Medal*, and in whose honor this special issue is dedicated, UVPD of iodotyrosine leads rise to efficient distonic cleavage of the C–I bond (see Scheme 1) [8]. This radical can then undergo radical rearrangement reactions to drive subsequent dissociation chemistry in so-called radical-directed dissociation (RDD) [9]. Since fragmentation occurs on the peptide backbone, it is generally thought that this is preceded by hydrogen abstraction of one of the backbone hydrogens.

Structural insights into the reaction chemistry of radical ions can come from action spectroscopy techniques, such as infrared multiple photon dissociation (IRMPD) spectroscopy [24] and UV spectroscopy [25]. The hydrogen stretching region in particular can give insights into hydrogen atom/proton rearrangements [26, 27], while UV spectroscopy can probe the generation [28, 29] and/or the structures of radical species [30, 31].

The aim of this study is to explore the UVPD fragmentation chemistry of the simple related molecular systems tyrosine, *iodo*tyrosine, and *diiodo*tyrosine, in their protonated forms. Experimentally derived fragmentation kinetics and infrared spectra of the product ions, in combination with a theoretical investigation of the potential energy surfaces of putative rearrangement reactions, yield mechanistic insights into the reactions that take place.

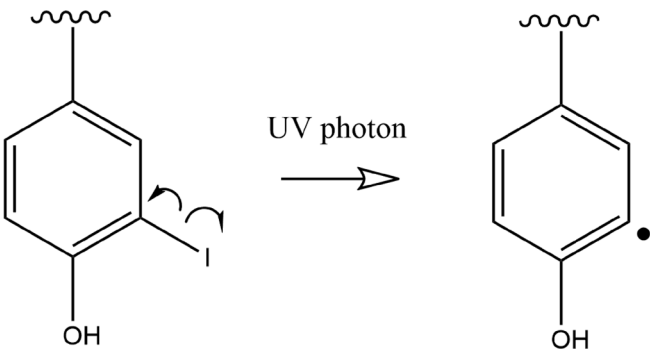

Scheme 1. Generation of radical site at known location via distonic cleavage of photolabile C–I bond

Experimental and Theoretical Methods

Mass Spectrometry

The chemicals tyrosine, iodotyrosine, and diiodotyrosine come from commercial sources (Sigma Aldrich, St. Louis, MO). Electrospray ionization (ESI) solutions of 10^{-4} M are dissolved in H_2O:CH_3OH:HCOOH (49:49:2). These solutions are introduced into a custom mass spectrometer described previously [32, 33]. ESI-generated ions are accumulated in a hexapole, prior to extraction via a quadrupole mass filter (QMF) for mass selection, and subsequent introduction into a quadrupole ion trap (QIT). Here, ions can be trapped for variable periods of time, prior to pulsed extraction into a time-of-flight (ToF) drift tube for mass analysis. The UVPD and infrared multiple photon dissociation (IRMPD) spectroscopy experiments conducted on the ions in the QIT are described below.

UVPD

Mass-selected precursor ions are subjected to one intense pulse (8 ns, 7 mJ) from an ArF excimer laser at a fixed wavelength of 193 nm (GAM, Model EX5-1000 Hz, Orlando, FL). The time delay (ΔT) between laser irradiation and extraction of the ions into the ToF drift tube is controlled and monitored using the setup depicted in Fig. 1, described in detail below. The reason for this complicated time control setup is the considerable time jitter in triggering the laser and ion extraction. In order to obtain UVPD mass spectra at a high time precision (i.e., resolved on a nanosecond timescale), each mass spectrum with its corresponding ΔT must be recorded separately. Mass spectra are then later binned together in ΔT time steps ± 5 ns, so that averaged mass spectra (i.e., at least 100 averages) with a higher signal-to-noise (S/N) can be visualized.

The sequence of events in Fig. 1 is as follows. A delay generator (Stanford Research Systems, DS645) is triggered by a LabView program from the computer workstation. Two outgoing pulses (orange) then trigger both the ArF excimer laser and rf power supply that drives the QIT. A photodiode (Electro-Optics Technology Inc., Traverse City, MI) is used to track the UV laser pulse output (purple), which is recorded (red) by an oscilloscope (Rigol Technology Inc., Beaverton, OR). When triggering the rf power supply (Jordan ToF Products, Grass Valley, CA), the rf amplitude is quickly dampened (~ 1 cycle), which then triggers application of high DC voltages on both entrance (+ 900 V) and exit (− 900 V) electrodes on the QIT, for extracting the ions into the ToF drift tube. The application of this extraction voltage (green) is recorded by the oscilloscope. The time difference between laser irradiation (red) and ion extraction (green) into the ToF, ΔT (blue), is finally communicated to the LabView software on the computer workstation, along with the corresponding digitized UVPD mass spectrum from the ToF mass analyzer (black). Note that the time resolution of the ΔT measurement is ± 1 ns, and it is limited by the digitization rate of the oscilloscope (i.e., Gs/s for all channels, so 500Ms/s for two channels).

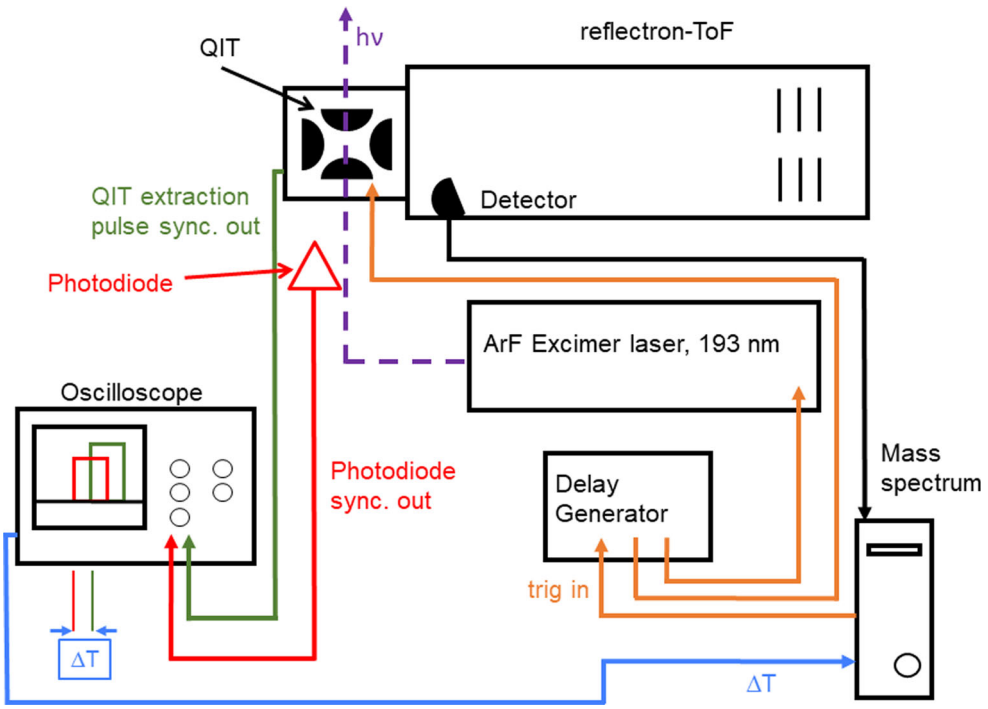

Figure 1. Schematic of the setup to control and monitor the time delay between laser irradiation and ion extraction from the QIT into the ToF drift tube

IRMPD Spectroscopy

UVPD product ions that are stable on longer timescales are mass isolated inside the QIT using the apex isolation method [33], where a DC voltage is applied to the ring electrode (for 30 ms). After a further cool-down delay (~ 50 ms), the selected UVPD product is irradiated with the tunable output from an optical parametric oscillator/amplifier (OPO/A) (Laser Vision, Bellevue, WA), followed by extraction of the remaining UVPD product ion and its IRMPD photofragments. This procedure is repeated for a range of IR wavelengths. By plotting the IRMPD yield as a function of OPO/A wavelength, the IRMPD spectrum of an ion can be obtained [34, 35].

Quantum Chemical Calculations

The structures corresponding to stationary points on the potential energy surfaces (PESs) are computed using the B3LYP DFT functional [36, 37] and the 6-311++G** basis set [38, 39]. The zero-point vibrational energy (ZPE) corrections are also performed at the B3LYP/6-311++G** level of theory. The calculations utilize spin-polarized Kohn-Sham reference states, using the *NWChem* program [40].

The stationary point structures have been connected through intrinsic reaction coordinates that involve one-step and, for the most part, energetically feasible processes: 1,3-proton shifts, bond rotations, and metastable ring formations (in case of some first-order saddle points). The common energy reference point for all three pathways is the rotational isomer (formed by rotation around the phenol O–H bond at the aromatic ring) of the protonated radical expected to form immediately after the distonic $I^{\bullet}$ loss.

For the comparison to the experimental IRMPD spectra, frequency calculations of putative candidate structures are carried out at the B3LYP/6-31+G* level of theory for the same minima found at the B3LYP/6-311++G** level. As shown in a similar study on protonated tryptophan [41] and previously on tryptamine [42], this level of theory in combination with recommended scaling factors for OH (0.976), NH (0.959), and CH (0.961), was able to closely reproduce the experimental band positions.

Results and Discussion

Overview of Photodissociation Pathways

Putative fragmentation pathways of the related protonated molecules tyrosine, *iodo*tyrosine, and *diodo*tyrosine are summarized in Scheme 2. This scheme is not meant to be a comprehensive summary of all of the competing fragmentation pathways. Rather, the scheme illustrates that there may be a number of competing and sequential fragmentation pathways. The loss of H_2O and CO has been studied in detail previously by Siu and co-workers [43], indicating that this likely takes place as a concomitant loss of both neutral molecules (shown mechanistically for H_2O and CO loss in tyrosine). Assuming that a single UV photon at 193 nm is absorbed, this corresponds to a total energy of 6.42 eV (148 kcal/mol, 620 kJ/mol). This is in excess of an estimated C–I bond energy on the order of ~ 280 kJ/mol (67 kcal/mol) [44] and an activation barrier of ~ 36 kcal/mol (151 kJ/mol) for the concomitant H_2O and CO loss [43, 45]. In fact, even the energy of a 266-nm photon (4.66 eV, 107 kcal/

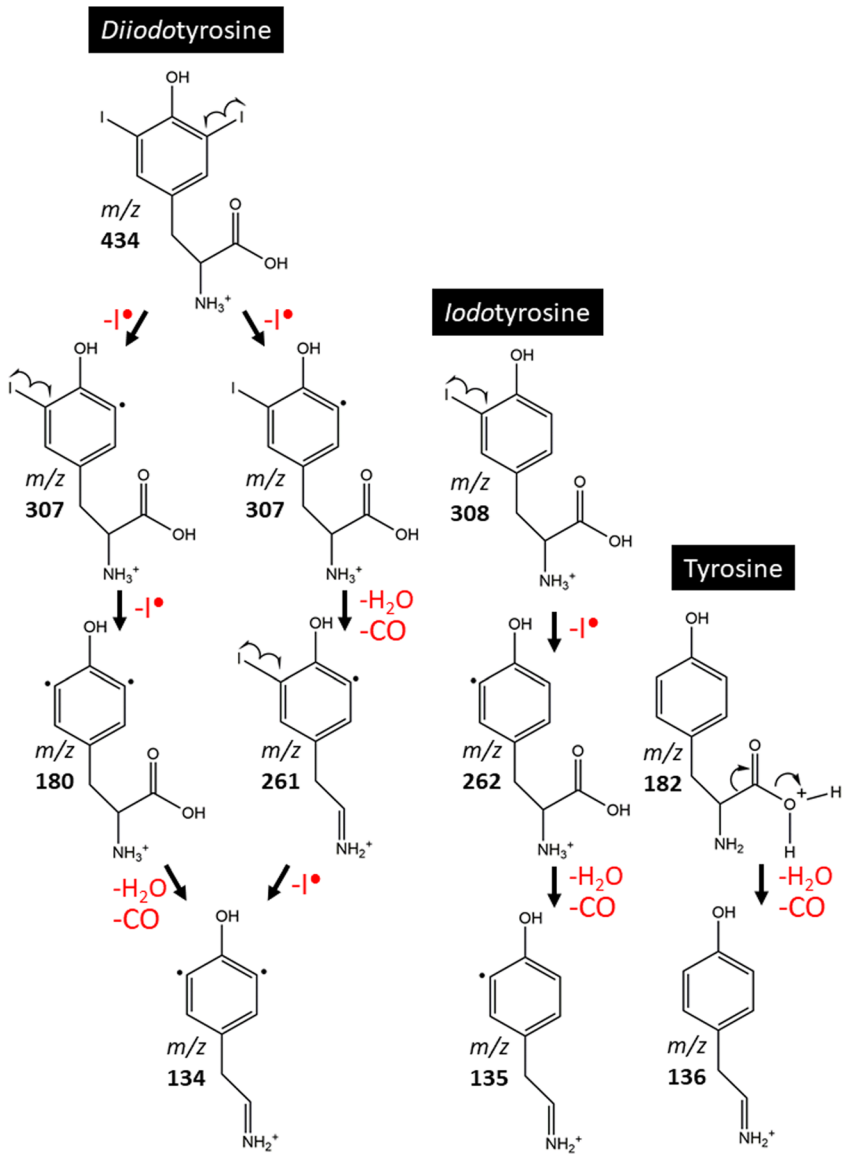

Scheme 2. Putative fragmentation pathways of protonated *diiodo*tyrosine, *iodo*tyrosine, and tyrosine

mol, 450 kJ/mol) is (slightly) in excess of these photodissociation pathways, even though this is not studied here.

Metastable Fragmentation

In order to get an understanding of the sequential nature of the fragmentation chemistry, it can be insightful to consider changing the timescale of ion detection relative to laser-induced photodissociation. Figure 2 shows the UVPD mass spectra of protonated *diiodo*tyrosine at different delay times between laser irradiation and QIT ion extraction, namely 10 ns and 10 ms. There are appreciable differences between both UVPD mass spectra, which are indicative of photodissociation chemistry that takes place at longer timescales (i.e, µs and ms). Some effects are trivial, such as the appearance of lower *m/z* ions in the 10 ns UVPD mass spectrum. These ions are at *q* values that are too large to be trapped and thus will not appear in the 10 ms UVPD mass spectrum. As a sidenote, not all ions observed arise from UVPD, as photoionization of neutral background molecules also contributes to the mass spectrum. Other trends are more telling about the sequential dissociation chemistry. For instance, the *m/z* 307 UVPD product, which results from iodine loss from *diiodo*tyrosine, appears at short times (10 ns), but almost disappears in the 10 ms UVPD mass spectrum. This suggests that *m/z* 307 is an initial UVPD product that then subsequently dissociates to consecutive products. A timescale of 10 ms is considered to be long on a dissociation dynamics timescale [46]. If the photodissociation takes place on lifetimes of µs or even ns, and thus on the timescales of ToF mass separations, this would be considered metastable fragmentation. Metastable processes are known to have an effect on the ToF peak shapes in UVPD [47], as well as mass detection in ion traps [48].

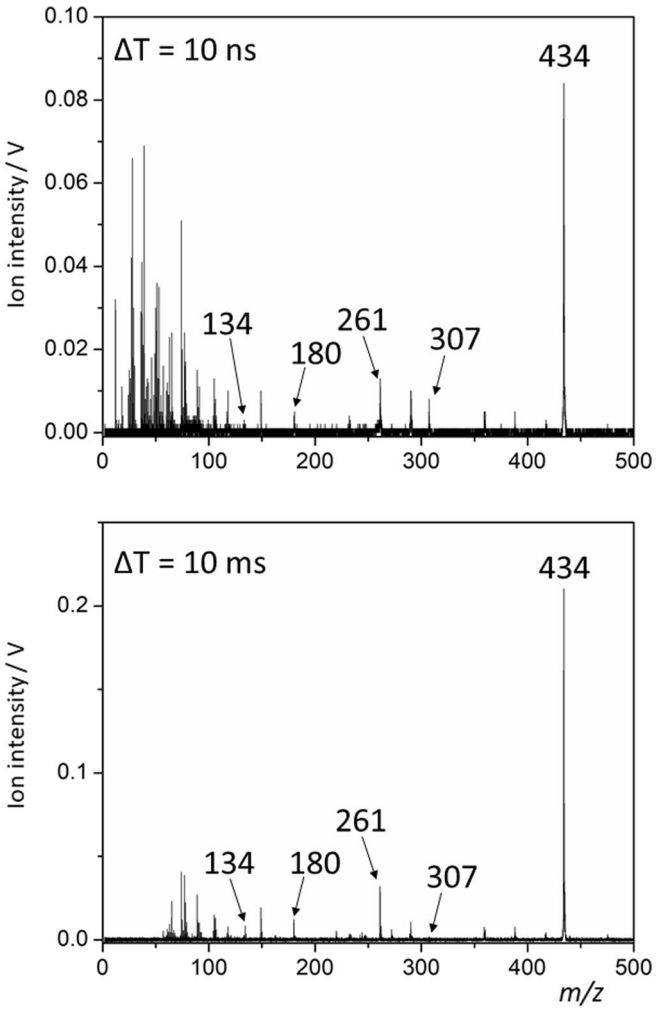

Figure 2. UVPD mass spectra of protonated *diiodo*tyrosine for time delay between laser irradiation and ion extraction ΔT = 10 ns and ΔT = 10 ms

Figure 3 shows the ToF distributions of the precursor *m/z* 434, as well as the photofragments *m/z* 307 and 261, for different ΔT delay times. As the precursor never changes in *m/z*, its ToF distribution is independent of ΔT. Conversely, for the photofragment *m/z* 261, there are considerable differences in the ToF distributions, with small ΔTs (90 ns) showing asymmetric peak shapes with long tails. These tails result from metastable dissociation. As a precursor ion is excited by UV photons, it may photodissociate *during* ion extraction/acceleration. This effectively means that the ion is accelerated for some time as the precursor ion, but after fragmentation, it is accelerated as the fragment ion. As the precursor ion is higher in mass, the resulting velocity of the photofragment is *lower* than it would be if it were the photofragment for the whole duration of the acceleration. It follows that those metastable ions have later arrival times at the detector, giving rise to the tail at longer ToFs. Interestingly, the UVPD product *m/z* 307 does not seem to indicate any metastable fragmentation, which suggests that its fragmentation is very fast, faster than the ns time resolution that can be achieved here. In other words, UVPD to *m/z* 307 must be considered instantaneous on the timescale of the experiment, and this is consistent with the ultrafast dissociation dynamics of iodobenzene (< ps) [49]. The ToF distributions for the UVPD products *m/z* 180 and 134 are shown in the Supplementary Materials (Fig. S1). The S/N for those mass spectra is somewhat lower, given their lower yields. Nonetheless, evidence for metastable decay can be discerned.

Simulating the ToF distributions in a reflectron ToF mass analyzer is not trivial, as there are many contributing factors (e.g., initial KE distribution, kinetic energy release, dissociation lifetime, and reflectron settings) [47]. Instead, we will employ a more visual approach to analyze ToF distributions. It is expected that the asymmetry of the ToF peak, which is due to the metastable population, is maximized at short ΔT. Conversely, the metastable contribution should decrease to zero at long ΔT, leading to a fully symmetric peak. By taking the central line around the symmetric ToF distribution at long times (i.e., at ΔT = 10 ms) as a reference, we can define left and right parts of the peak. For symmetric peaks, the percentage ratio right/(left + right) = 50%, whereas for asymmetric peaks with metastable population, the percentage ratio right/(left + right) > 50% (see inset Fig. 3).

Figure 4 shows the plot of the right/(left + right) percentage ratio as a function of ΔT. Some ratios start off at values > 50%, but then decrease to 50% for larger values of ΔT. This is consistent with the anticipated trends that when ΔT is increased, more ions fragment prior to ion extraction, meaning that the relative fraction of the metastable population decreases, and the percentage ratio right/(left + right) approaches 50%. As a control, the ratio for the precursor ion *m/z* 434 always stays at 50% (as would in fact be expected). Similarly, the percentage ratio for the iodine loss UVPD product (at *m/z* 307) also remains at 50% throughout. This again confirms that this photodissociation channel is very fast. The photofragments at *m/z* 261, 180, and 134 all exhibit asymmetric peak shapes for hundreds of ns. While the standard deviations are appreciable, the trend lines unambiguously decrease over time, approaching 50% asymptotically. The intermediate fragments, *m/z* 180 and 261, have very similar trend lines, whereas the smallest UVPD product, *m/z* 134, displays a less steep curve, indicative of a slower metastable dissociation behavior. This is consistent with *m/z* 134 being a sequential dissociation product from either the *m/z* 180 and 261 products (Scheme 2).

While these time plots are instructive to distinguish between faster and slower processes, one should not overinterpret the data to extrapolate lifetimes for the slower UVPD processes. The maximum-attainable percentage ratio in Fig. 4 is/are dependent on the lifetime(s) of the photodissociation process(es), the mass shift (upon fragmentation), and the many experimental variables (acceleration voltages, reflectron settings). Even more importantly, it is debatable how this type of kinetic data would fit into the larger picture of UVPD dissociation dynamics. In the present experiments, the UVPD ion signal needed to be maximized for S/N considerations, and thus the photon flux

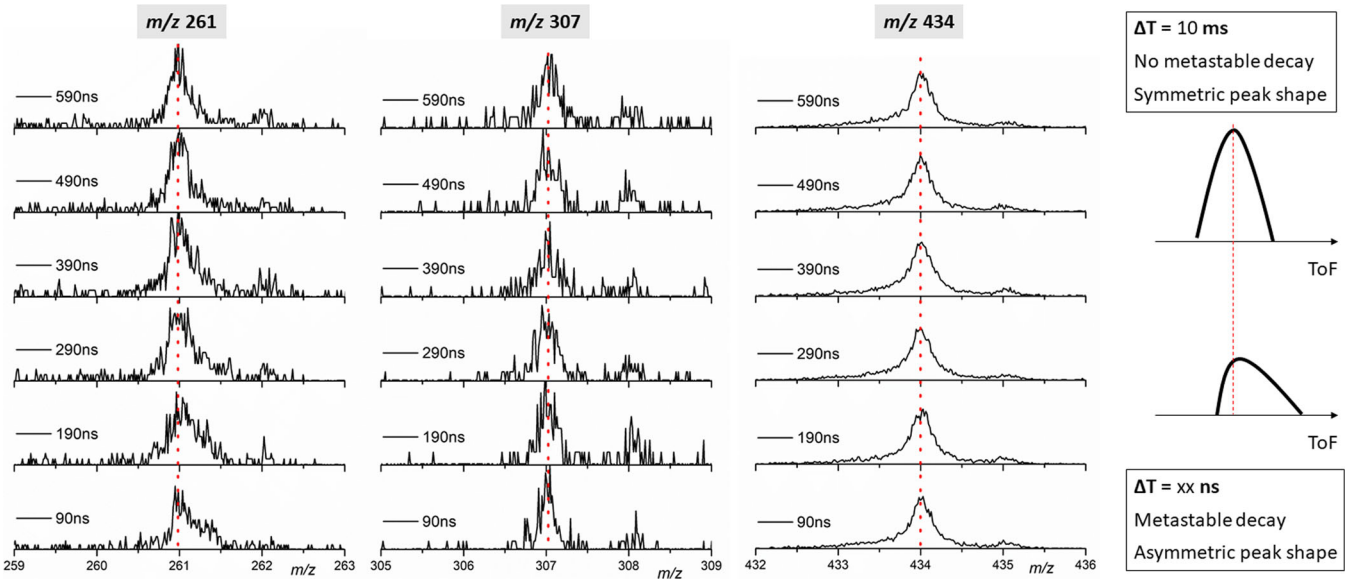

Figure 3. ToF peaks for *m/z* 261, 307, and 434 at different time delays ΔT (90–590 ns). Inset on the right schematically shows symmetry and asymmetry of ToF distribution depending on the presence of metastable decay. Red dashed line indicates reference ToF for symmetric peak at ΔT = 10 ms.

is too large to obey a single-photon absorption regime. In other words, precursor ions may absorb a different number of photons (one, two, or even more), giving rise to very broad energy distributions, and thus cannot satisfy single kinetic rate conditions. The experimental data largely corroborates this hypothesis. The UVPD dissociation dynamics span orders of magnitude in time. All UVPD product channels are observed even at very small time delays (see ΔT = 10 ns, Fig. 2), so in fact the appearance of these fragments is coincident with UV irradiation. Some fragments display metastable dissociation on the hundreds of ns timescales, but their yields increase even further on the μs and ms timescales. This type of behavior is compatible with an evaporative ensemble [50], where progressively the photodissociation dynamics of cooler ions are probed.

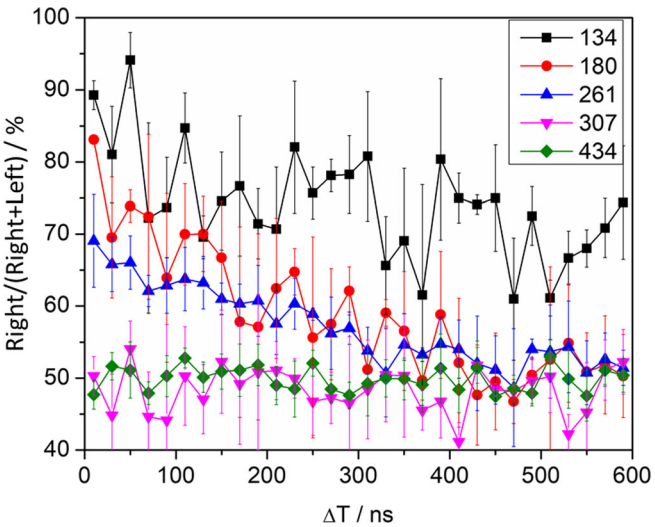

Figure 4. Right/(left + right) percentage ratios as a function of ΔT for the precursor *m/z* 434, and various UVPD product ions, at *m/z* 134, 180, 261, and 307

IRMPD Spectroscopy

In the UVPD chemistry in Scheme 2, three related UVPD products are generated from either precursor, the closed-shell fragment *m/z* 136, the radical fragment *m/z* 135, and the nominal biradical at *m/z* 134. We will investigate the structures of these product ions based on experimental IRMPD spectra that are compared to theoretical calculations of putative structures.

Figure 5 summarizes the experimental results and shows the identified rearrangement structures based on a match of their computed IR spectra with the experiment. The detailed potential energy surfaces (PESs) for these hydrogen atom/proton rearrangements will be discussed further below.

For the closed-shell *m/z* 136 product ion, the fairly simple hydrogen stretching pattern of three bands matches the putative structure fairly well. The spectrum consists of the free phenol OH stretch at 3650 cm^{-1}, an asymmetric NH_2^+ stretch at 3445 cm^{-1}, and a symmetric NH_2^+ stretch at 3250 cm^{-1}. Note that in this case, the structure of the product ion is unambiguous, and the purpose of this control experiment is exclusively to observe how closely theory is able to match experiment. In Fig. S2 in the Supplementary Materials, the different basis sets 6-311++G** and 6-31+G* are contrasted in terms of their match with the experiment. For 6-311++G**, a recommended uniform scaling factor (0.9689) is employed [51], as opposed to individual scaling factors for OH (0.976) and NH (0.959) in the case of 6-31+G*. The match for the larger basis set is very poor, and it would be difficult to confirm the structure in this way. Conversely, the match for 6-31+G* is much better, as also

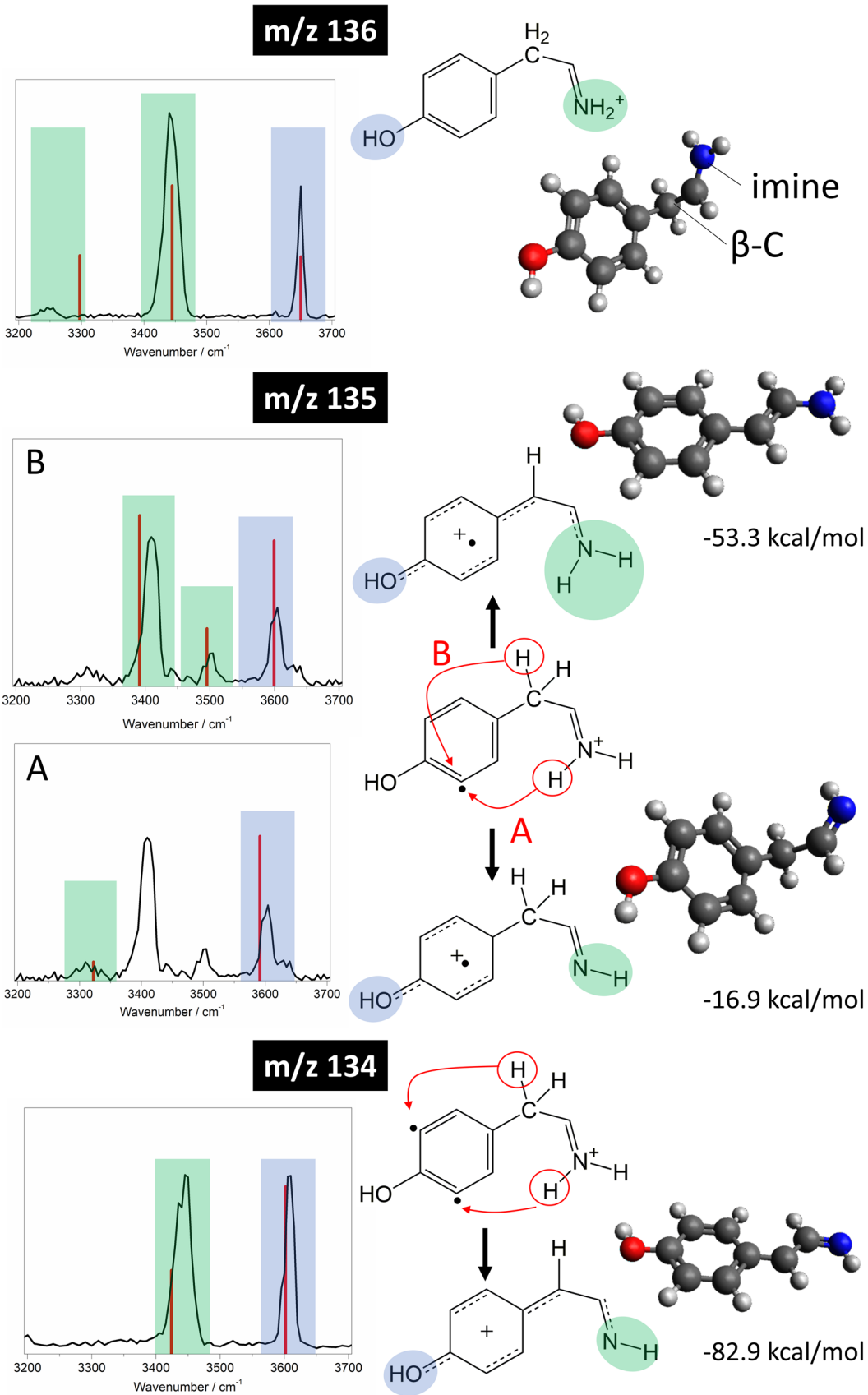

Figure 5. Comparison of experimental IRMPD spectral for UVPD products *m/z* 136, 135, and 134 with matched computed structures and IR spectra. Stick structures indicate proton rearrangements, resonance stabilization, and relative energies. Band assignments are indicated by color coding

shown in previous studies [41, 42]. This is an only too common observation for DFT, where larger basis sets do not necessarily translate into a better match with experiment.

The bottom IRMPD spectrum for the nominal biradical *m/z* 134 product is surprisingly simple, exhibiting only two experimental bands. This simple pattern is reproduced by a putative rearrangement structure, involving two proton transfers, an imine hydrogen, and a β-C hydrogen. In the resulting structure, the π electron cloud is fully delocalized over the whole molecule (due to hydrogen abstraction from the β-C), and the structure is planar. The phenol OH stretch is now redshifted to 3600 cm^{-1}, which is consistent with the charge being delocalized on the aromatic ring. Moreover, the appearance of a single NH stretch at 3450 cm^{-1} is decidedly consistent with the proposed structure. Energetically, the double proton rearrangement structure is significantly favored (−82.9 kcal/mol). Note that the relative energy uses the triplet radical as a precursor, rather than the singlet state. As shown in Fig. S3 in the Supplementary Materials, though the singlet is lower in energy in this case, it involves a loss of aromaticity, due to a rearrangement of the ring structure. Such a non-aromatic structure may preclude proton rearrangements. At this point, it is an open question whether a biradical structure is really formed, or whether the sequence of events involves distonic $I^{\bullet}$ loss, followed by proton transfer, followed by another distonic $I^{\bullet}$ loss and proton transfer.

The middle IRMPD spectrum of the single radical *m/z* 135 product ion displays the largest number of features, which cannot be reconciled with a single structure. Thus, two proton rearrangement product ion structures are proposed, involving either transfer of an imine hydrogen (structure A), or transfer of a β-C hydrogen (structure B). A mixture of these product ion structures can rationalize appearance of the bands at 3320, 3420, and 3505 cm^{-1}, respectively being assigned to the imine NH stretch, symmetric NH_2^+ stretch, and asymmetric NH_2^+ stretch. The redshifted phenol OH stretch at 3600 cm^{-1} is again indicative of the charge being delocalized on the aromatic ring. Note on this point that in structure A, the charge is delocalized over the aromatic ring, whereas in structure B, it is delocalized over the whole molecule, thus explaining the more blueshifted OH stretch in B.

Computed Rearrangement Pathways

While proton migration from the protonated imine group is easy to rationalize, the proton/hydrogen atom transfer from the β-C is arguably not as straightforward to understand. In the latter case, it may be a question of semantics as to whether to call these transfers proton or hydrogen atom migrations. For the purpose of simplicity, we will refer to these rearrangements as proton rearrangements, as a proton migrates either with or without corresponding transfer of electron density.

In this very simple molecular system, it is conceivable that there would be a preferred rearrangement pathway. Figure 6 summarizes three pathways to rationalize the appearance of the experimentally confirmed structures A and B (Fig. 5). The various protons are color-coded to make it easier to follow various rearrangement pathways. The detailed potential energy surfaces (PESs) for these rearrangement pathways are given in the Supporting Information in Figs. S4–S6, and information on the absolute energies of these structures can be found in Table S1.

In the first pathway, the phenol proton is first transferred to occupy the radical site on the aromatic ring (as originally suggested in the literature [8]). An imine proton then migrates to replenish the phenol OH, leading to structure A. A 1,3-shift-type isomerization reaction, involving a proton transfer from the β-C to the imine, could then rationalize appearance of structure B. In the case of pathway 1, while there are practically equivalent pathways through combination of rotation around the C–C bond in the side-chain and the transfer of a proton from the phenol O to the C (from the distonically cleaved C–I bond) in the aromatic ring, two differing sub-paths to product A appear (see Fig. S4, Supplementary Materials). One is through the direct proton transfer, via significant distortion of the aromatic ring, between the protonated amine N and the phenoxy O through a transition state involving seven members (21.9 kcal/mol). The second occurs through unstable saturation of one of the carbons in the aromatic ring (46.5 kcal/mol). The first subpathway is energetically favorable by ~ 25 kcal/mol, involves one less intermediate, and is therefore expected to be dominant. The 1,3-shift isomerization proceeds via transfer first to the α-C, then the NH group. Structure B consists of all-sp^2 hybridized carbons, and thus the charge is delocalized over the entire molecule in a planar configuration. This also explains the very favorable energetics of structure B.

In pathway 2, there is a nearly direct transfer of the imine proton to the radical site on the aromatic ring via the π cloud on the aromatic ring (Fig. S5, Supplementary Materials). This is achieved by bending the imine chain, and thus structure A is formed directly. An alternative transition state (44.7 kcal/mol), involving the migrating proton between the two aromatic carbons, could not be confirmed. Once again, a 1,3-shift-type isomerization could explain the appearance of structure B. In pathway 3, a β-carbon proton is able to effectively "hop" on the aromatic ring to the radical site (Fig. S6). Such a mechanism could explain structure B, but not structure A. Surprisingly, mechanism 3 exhibits the lowest barriers overall.

Because all the distinct reaction pathways involve activation barriers of similar magnitude (each pathway has at least one activation barrier of ~ 40 ± 3 kcal/mol), none of the pathways are expected to be energetically preferred for the intramolecular proton migration, and it is conceivable that all pathways operate in parallel. As pathway 3 cannot rationalize the appearance of structure A, pathways 1 and/or 2 are required. The considerable barrier in the 1,3-shift isomerization reaction (in pathways 1 and 2) is compatible with the fact that both structures A and B are observed. For a sizeable fraction of the ion population, there would be insufficient internal energy to overcome this barrier, and thus structure A would be the end point of the reaction.

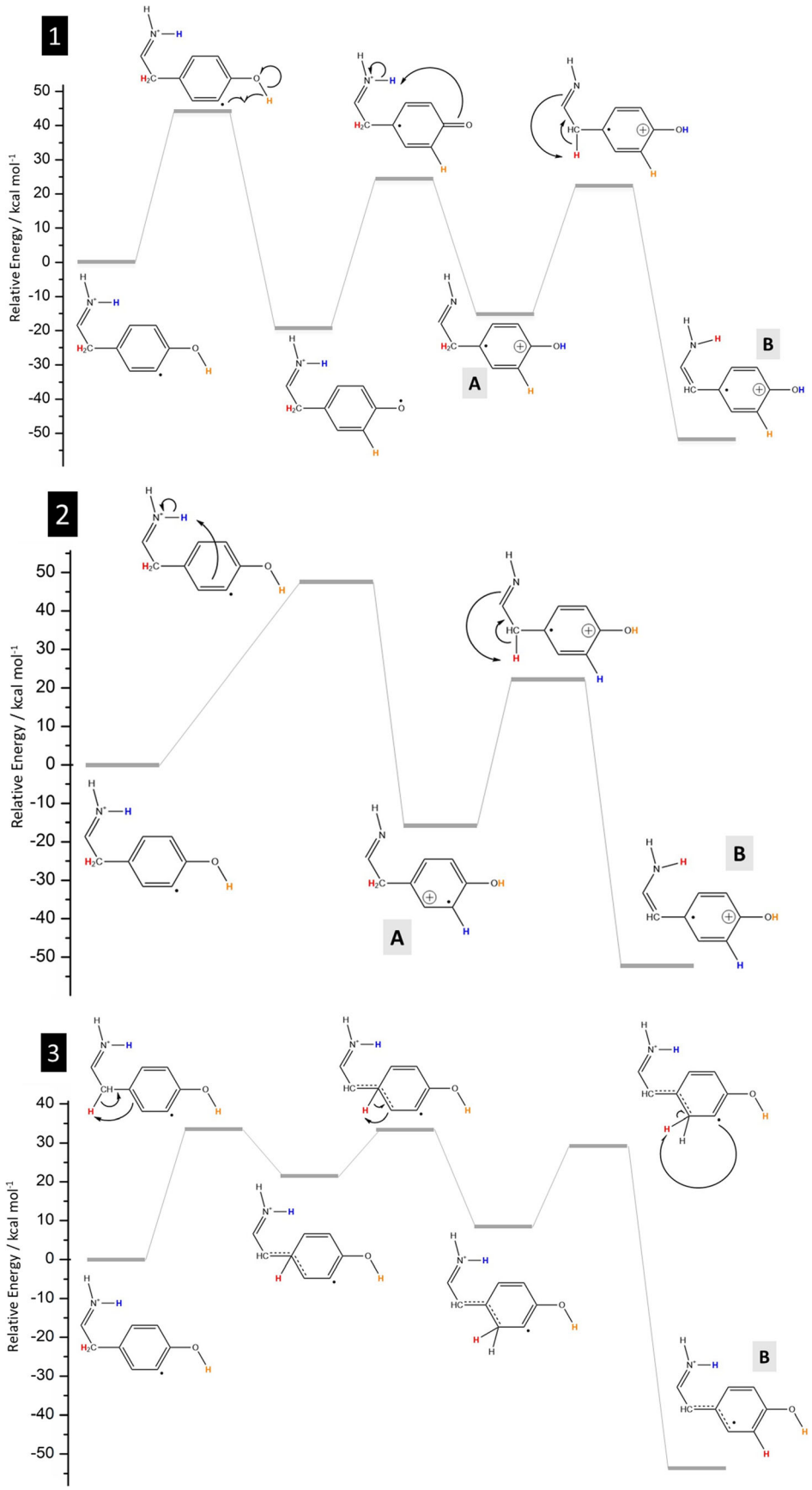

Figure 6. Summary of proton rearrangement pathways, showing key transition states and intermediate products. More detailed pathways are given in Supplementary Materials (Fig. S4–S6)

Conclusions

This study has focused on a mechanistic understanding of the dissociation chemistry of iodinated tyrosine systems under ultraviolet irradiation. By controlling the time delay between UV irradiation and ion extraction into a ToF drift tube, some of the qualitative kinetics of UVPD can be teased out on ns timescales. It is thus confirmed that the distonic $I^{\bullet}$ loss is extremely fast (occurring within the UV irradiation pulse). Conversely, a consecutive $I^{\bullet}$ loss and/or concomitant neutral losses (i.e., H_2O and CO) show up as metastable decay, leading to asymmetric ToF peak shapes. IRMPD spectra of related UVPD product ions exhibit distinct NH stretching signatures in the hydrogen stretching region, verifying which rearrangement reactions took place. In *diiodo*tyrosine, where two radical sites are generated on the aromatic ring, two proton transfers occur, involving one of the imine hydrogens and one of the β-C hydrogens. In *iodo*tyrosine, where one radical site is created on the aromatic ring, two structures are observed, involving either transfer of an imine or of a β-C hydrogen. Based on computed potential energy surfaces, it is sobering to note, however, that even in these simple molecular systems, multiple reaction pathways may be at play. This suggests that the fragmentation chemistry in UVPD of larger peptides or even proteins is extremely complex, likely resulting in a cascade of rearrangement reactions.

Funding Information

The project was financially supported by the United States National Science Foundation (NSF) under grant number CHE-1403262.

References

1. Turecek, F., Julian, R.R.: Peptide radicals and cation radicals in the gas phase. Chem. Rev. **113**, 6691–6733 (2013)
2. Zubarev, R.A., Kelleher, N.L., McLafferty, F.W.: Electron capture dissociation of multiply charged protein cations. A nonergodic process. J. Am. Chem. Soc. **120**, 3265–3266 (1998)
3. Mirgorodskaya, E., Roepstorff, P., Zubarev, R.A.: Localization of O-glycosylation sites in peptides by electron capture dissociation in a Fourier transform mass spectrometer. Anal. Chem. **71**(20), 4431–4436 (1999)
4. Syka, J.E.P., Coon, J.J., Schroeder, M.J., Shabanowitz, J., Hunt, D.F.: Peptide and protein sequence analysis by electron transfer dissociation mass spectrometry. Proc. Natl. Acad. Sci. U. S. A. **101**, 9528–9533 (2004)
5. Mikesh, L., Ueberheide, B., Chi, A., Coon, J., Syka, J.E.P., Shabanowitz, J., Hunt, D.F.: The utility of ETD mass spectrometry in proteomic analysis. Biochim. Biophys. Acta - Prot. Proteom. **1764**, 1811–1822 (2006)
6. Robinson, M.R., Moore, K.L., Brodbelt, J.S.: Direct identification of tyrosine sulfation by using ultraviolet photodissociation mass spectrometry. J. Am. Soc. Mass Spectrom. **25**, 1461–1471 (2014)
7. Parthasarathi, R., He, Y., Reilly, J., Raghavachari, K.: New insights into the vacuum UV photodissociation of peptides. J. Am. Chem. Soc. **132**, 1606–1610 (2010)
8. Ly, T., Julian, R.R.: Residue-specific radical-directed dissociation of whole proteins in the gas phase. J. Am. Chem. Soc. **130**, 351–358 (2008)
9. Ly, T., Julian, R.R.: Elucidating the tertiary structure of protein ions in vacuo with site specific photoinitiated radical reactions. J. Am. Chem. Soc. **132**, 8602–8609 (2010)
10. Brodbelt, J.S.: Photodissociation mass spectrometry: new tools for characterization of biological molecules. Chem. Soc. Rev. **43**, 2757–2783 (2014)
11. Fung, Y., Kjeldsen, F., Silivra, O., Chan, T., Zubarev, R.A.: Facile disulfide bond cleavage in gaseous peptide and protein cations by ultraviolet photodissociation at 157 nm. Angew. Chem. Int. Ed. Engl. **44**, 6399–6403 (2005)
12. Hunt, D.F., Shabanowitz, J., Yates John 3rd, R.: Peptide sequence analysis by laser photodissociation Fourier transform mass spectrometry. J. Chem. Soc. Chem. Commun. **8**, 548–550 (1987)
13. Williams, E.R., Furlong, J.J.P., McLafferty, F.W.: Efficiency of collisionally-activated dissociation and 193-nm photodissociation of peptide ions in Fourier transform mass spectrometry. J. Am. Soc. Mass Spectrom. **1**, 288–294 (1990)
14. Julian, R.R.: The mechanism behind top-down UVPD experiments: making sense of apparent contradictions. J. Am. Soc. Mass Spectrom. **28**, 1823–1826 (2017)
15. Syrstad, E.A., Turecek, F.: Toward a general mechanism of electron capture dissociation. J. Am. Soc. Mass Spectrom. **16**, 208–224 (2005)
16. Sobczyk, M., Anusiewicz, W., Berdys-Kochanska, J., Sawicka, A., Skurski, P., Simons, J.: Coulomb-assisted dissociative electron attachment: application to a model peptide. J. Phys. Chem. A. **109**, 250–258 (2005)
17. Thoen, K.K., Perez, J., Ferra, J.J., Kenttamaa, H.I.: Synthesis of charged phenyl radicals and biradicals by laser photolysis in a Fourier transform ion cyclotron resonance mass spectrometer. J. Am. Soc. Mass Spectrom. **9**, 1135–1140 (1998)
18. Gauthier, J.W., Trautman, T.R., Jacobson, D.B.: Sustained off-resonance irradiation for collision-activated dissociation involving Fourier-transform mass-spectrometry—collision-activated dissociation technique that emulates infrared multiphoton dissociation. Anal. Chim. Acta. **246**, 211–225 (1991)
19. Chu, I.K., Rodriguez, C.F., Lau, T.C., Hopkinson, A., Siu, K.: Molecular radical cations of oligopeptides. J. Phys. Chem. B. **104**, 3393–3397 (2000)
20. Hao, G., Gross, S.: Electrospray tandem mass spectrometry analysis of S- and N-nitrosopeptides: facile loss of NO and radical-induced fragmentation. J. Am. Soc. Mass Spectrom. **17**, 1725–1730 (2006)
21. Gallardo, V.A., Jankiewicz, B.J., Vinueza, N.R., Nash, J.J., Kenttamaa, H.I.: Reactivity of a σ,σ,σ,σ-tetraradical: the 2,4,6-trihydropyridine radical cation. J. Am. Chem. Soc. **134**, 1926–1929 (2012)
22. Heidbrink, J.L., Ramirez-Arizmendi, L.E., Thoen, K.K., Guler, L., Kenttamaa, H.I.: Polar effects control hydrogen-abstraction reactions of charged, substituted phenyl radicals. J. Phys. Chem. A. **105**, 7875–7884 (2001)
23. Marconi, G.: Model for the photodissociation of aryl halides. J. Photochem. **11**, 385–391 (1979)
24. Polfer, N.: Infrared multiple photon dissociation spectroscopy of trapped ions. Chem. Soc. Rev. **40**, 2211–2221 (2011)
25. Antoine, R. and P. Dugourd, UV-visible activation of biomolecular ions. In: Polfer, N.C., Dugourd, P. (eds.) Laser Photodissociation and Spectroscopy of Mass-Separated Biomolecular Ions, pp. 93–116. Springer: Lect. Notes Chem., Vol. 83, (2013)
26. Lesslie, M., Lawler, J.T., Dang, A., Korn, J.A., Bim, D., Steinmetz, V., Maitre, P., Turecek, F., Ryzhov, V.: Cytosine radical cations: a gas-phase study combining IRMPD spectroscopy, UVPD spectroscopy, ion-molecule reactions, and theoretical calculations. Chem. Phys. Chem. **18**, 1293–1301 (2017)
27. Osburn, S., Berden, G., Oomens, J., Gulyuz, K., Polfer, N.C., O'Hair, R.A.J., Ryzhov, V.: Structure and reactivity of the glutathione radical cation: radical rearrangement from the cysteine sulfur to the glutamic acid alpha-carbon atom. Chem. Plus Chem. **78**, 970–978 (2013)
28. Brunet, C., Antoine, R., Dugourd, P., Canon, F., Giuliani, A., Nahon, L.: Formation and fragmentation of radical peptide anions: insights from vacuum ultra violet spectroscopy. J. Am. Soc. Mass Spectrom. **23**, 274–281 (2012)
29. Kirk, B.B., Trevitt, A.J., Blanksby, S.J., Tao, Y.Q., Moore, B.N., Julian, R.R.: Ultraviolet action spectroscopy of iodine labeled peptides and proteins in the gas phase. J. Phys. Chem. A. **117**, 1228–1232 (2013)
30. Shaffer, S.A., Pepin, R., Turecek, F.: Combining UV photodissociation action spectroscopy with electron transfer dissociation for structure

analysis of gas-phase peptide cation-radicals. J. Mass Spectrom. **50**, 1438–1442 (2015)
31. Bellina, B., Compagnon, I., Houver, S., Maitre, P., Allouche, A.R., Antoine, R., Dugourd, P.: Spectroscopic signatures of peptides containing tryptophan radical cations. Angew. Chem. Int. Ed. Engl. **50**, 11430–11432 (2011)
32. Gulyuz, K., Stedwell, C.N., Wang, D., Polfer, N.C.: Hybrid quadrupole mass filter/quadrupole ion trap/time-of-flight-mass spectrometer for infrared multiple photon dissociation spectroscopy of mass-selected ions. Rev. Sci. Instrum. **82**, 054101 (2011)
33. March, R., Londry, F., Alfred, R., Franklin, A., Todd, J.: Mass-selective isolation of ions stored in a quadrupole ion trap—a simulation study. Int. J. Mass Spectrom. Ion Proc. **112**, 247–271 (1992)
34. Polfer, N., Oomens, J.: Vibrational spectroscopy of bare and solvated ions of biological significance. Mass Spectrom. Rev. **28**, 468–494 (2009)
35. Fridgen, T.D.: Infrared consequence spectroscopy of gaseous protonated and metal ion cationized complexes. Mass Spectrom. Rev. **28**, 586–607 (2009)
36. Stephens, P.J., Devlin, F.J., Chabalowski, C.F., Frisch, M.J.: Ab initio calculation of vibrational absorption and circular dichroism spectra using density functional force fields: a comparison of local, nonlocal, and hybrid density functional. J. Phys. Chem. **98**, 11623–11627 (1994)
37. Stephens, P.J., Devlin, F.J., Ashvar, C.S., Chabalowski, C.F., Frisch, M.J.: Theoretical calculations of vibrational circular-dichroism spectra. Fara. Disc. **99**, 103–119 (1994)
38. McLean, A.D., Chandler, G.S.: Contracted Gaussian-basis sets for molecular calculations. 1. 2nd row atoms, Z=11–18. J. Chem. Phys. **72**, 5639–5648 (1980)
39. Krichnan, R., Binkley, J.S., Seeger, R., Pople, J.A.: Self-consistent molecular orbital methods. 20. basis set for correlated wave-functions. J. Chem. Phys. **72**, 650–654 (1980)
40. Valiev, M., Bylaska, E.J., Govind, N., Kowalski, K., Straatsma, T.P., Van Dam, H.J.J., Wang, D., Nieplocha, J., Apra, E., Windus, T.L., de Jong, W.A.: NWChem: a comprehensive and scalable open-source solution for large scale molecular simulations. Comp. Phys. Commun. **181**, 1477–1489 (2010)
41. Mino, W.K., Gulyuz, K., Wang, D., Stedwell, C.N., Polfer, N.: Gas-phase structure and dissociation chemistry of protonated tryptophan elucidated by infrared multiple-photon dissociation spectroscopy. J. Phys. Chem. Lett. **2**, 299–304 (2011)
42. Nicely, A.L., Miller, D.J., Lisy, J.M.: Charge and temperature dependence of biomolecule conformations: K^+tryptamine-$(H_2O)_n$ clusters. J. Am. Chem. Soc. **131**, 6314–6315 (2009)
43. El Aribi, H., Orlova, G., Hopkinson, A., Siu, K.: Gas-phase fragmentation reactions of protonated aromatic amino acids: concomitant and consecutive neutral eliminations and radical cation formations. J. Phys. Chem. A. **108**, 3844–3853 (2004)
44. Blanksby, S.J., Ellison, G.B.: Bond dissociation energies of organic molecules. Acc. Chem. Res. **36**, 255–263 (2003)
45. O'Hair, R.A.J., Broughton, P.S., Styles, M.L., Frink, B.T., Hadad, C.M.: The fragmentation pathways of protonated glycine: a computational study. J. Am. Soc. Mass Spectrom. **11**, 687–696 (2000)
46. Laskin, J., Futrell, J.H.: Surface-induced dissociation of peptide ions: kinetics and dynamics. J. Am. Soc. Mass Spectrom. **14**, 1340–1347 (2003)
47. Weickhardt, C., Lifshitz, C.: Determination of kinetic-energy release distributions by metastable peak shape-analysis in an ion-trap reflectron time-of-flight instrument. Eur. Mass Spectrom. **1**, 223–228 (1995)
48. Pepin, R., Layton, E.D., Liu, Y., Afonso, C., Turecek, F.: Where does the electron go? Stable and metastable peptide cation radicals formed by electron transfer. J. Am. Soc. Mass Spectrom. **28**, 164–181 (2017)
49. Cheng, P.Y., Zhong, D., Zewail, A.H.: Kinetic-energy, femtosecond resolved reaction dynamics. Modes of dissociation (in iodobenzene) from time-velocity correlations. Chem. Phys. Lett. **237**, 399–405 (1995)
50. Hansen, K., The evaporative ensemble, in Statistical Physics of Nanoparticles in the Gas Phase, Springer: Atomic, Optical, and Plasma Physics, 73, p. 113–146 (2013)
51. Merrick, J.P., Moran, D., Radom, L.: An evaluation of harmonic vibrational frequency scale factors. J. Phys. Chem. A. **111**, 11683–11700 (2007)